

Collisional perturbation of radio-frequency E1 transitions in an atomic beam of dysprosium

A. Cingöz,^{1,*} A.-T. Nguyen,^{1,2} D. Budker,^{1,3,†} S. K. Lamoreaux,² and J. R. Torgerson²

¹*Department of Physics, University of California at Berkeley, Berkeley, California 94720-7300*

²*University of California, Los Alamos National Laboratory,*

Physics Division, P-23, MS-H803, Los Alamos, New Mexico 87545

³*Nuclear Science Division, Lawrence Berkeley National Laboratory, Berkeley, California 94720*

(Dated: July 30, 2021)

We have studied collisional perturbations of radio-frequency (rf) electric-dipole (E1) transitions between the nearly degenerate opposite-parity levels in atomic dysprosium (Dy) in the presence of 10 to 80 μ Torr of H₂, N₂, He, Ar, Ne, Kr, and Xe. Collisional broadening and shift of the resonance, as well as the attenuation of the signal amplitude are observed to be proportional to the foreign-gas density with the exception of H₂ and Ne, for which no shifts were observed. Corresponding rates and cross sections are presented. In addition, rates and cross sections for O₂ are extracted from measurements using air as foreign gas. The primary motivation for this study is the need for accurate determination of the shift rates, which are needed in a laboratory search for the temporal variation of the fine-structure constant [A. T. Nguyen, D. Budker, S. K. Lamoreaux, and J. R. Torgerson, Phys. Rev. A **69**, 22105 (2004)].

PACS numbers: 32.70.Jz, 32.30.Bv, 06.20.Jr

I. INTRODUCTION

Perturbations of atomic resonance lines by collisions with atoms were first observed by Michelson [1]. With the impact approximation, Lorentz [2] and Weisskopf [3] provided the earliest theoretical framework. While Lorentz treated the effects of collisions as a complete termination of a radiation wave train emitted by the atom, Weisskopf realized that a disruption in phase was sufficient to explain broadening. However, neither approach was able to explain shifts of the atomic resonances. Lindholm [4] and Foley [5] remedied this shortcoming with the adiabatic impact approximation theory which takes into account the effects of distant collisions that induce small phase changes ignored by Weisskopf. While this theory is able to predict the line shape near the resonance, the conditions necessary for its validity break down near the wings or at higher pressures where satellite lines and asymmetries have been observed. The initial theory for satellite lines, called the quasistatic approach, was developed by Khun [6]. In this approach, the motion of the perturber is ignored. The line shape is obtained by averaging the change in the energy difference between the atomic levels due to the presence of the perturber over the probability distribution of the stationary perturbers. However, this theory breaks down for frequencies near resonance or at low pressures. Since then, these failures have been alleviated by full quantum-mechanical treatments, developed to unify these two approaches. These techniques and related experiments are reviewed, for example, by Ch'en and Takeo [7], Allard and Kielkopf [8],

and Szudy and Baylis [9].

In this study, we investigate collisional perturbations of radio-frequency transitions between the nearly degenerate opposite parity levels of ¹⁶²Dy and ¹⁶³Dy (Z=66) due to the introduction of H₂, N₂, He, Ar, Ne, Kr, and Xe at pressure ranging from 10 to 80 μ Torr. While broadening and shift rates, and corresponding cross sections are presented for ¹⁶²Dy, only shift results are presented for ¹⁶³Dy due to large statistical uncertainties resulting from the dilution of the level population by hyperfine levels. Rates and cross sections due to O₂ are extracted from measurements using air as foreign gas. In addition, upper bounds on collisional-quenching cross sections are extracted from observations of the signal amplitude as a function of foreign-gas pressure.

The system under consideration is unusual for a collisional study since the foreign-gas pressures are \lesssim 80 μ Torr. In this pressure regime, the time between collisions is longer than the total transit time of the Dy atoms across the apparatus, assuming a typical cross section of 10^{-14} cm². The only other study of collisional perturbations in Dy that we are aware of was performed with a magnetic trap where the spin relaxation of the ground-state Zeeman sublevels due to He was presented [10].

The primary motivation for this study is the need for accurate determination of the shift rates which are important for a search for the temporal variation of the fine-structure constant, α [11]. Recently, evidence for variation in α on cosmological time scales was discovered in quasar absorption spectra [12, 13], corresponding to $\dot{\alpha}/\alpha = (6.40 \pm 1.35) \times 10^{-16}/\text{yr}$ assuming a linear shift over 10^{10} years [13]. The current terrestrial evidence comes from an analysis of fission products of a natural reactor in Oklo (Gabon) that operated 1.8×10^9 years ago, corresponding to $\dot{\alpha}/\alpha = (-2.3_{-0.4}^{+0.8}) \times 10^{-17}/\text{yr}$ [14]. However, observational measurements of this kind are

*Electronic address: acingoz@berkeley.edu

†Electronic address: budker@berkeley.edu

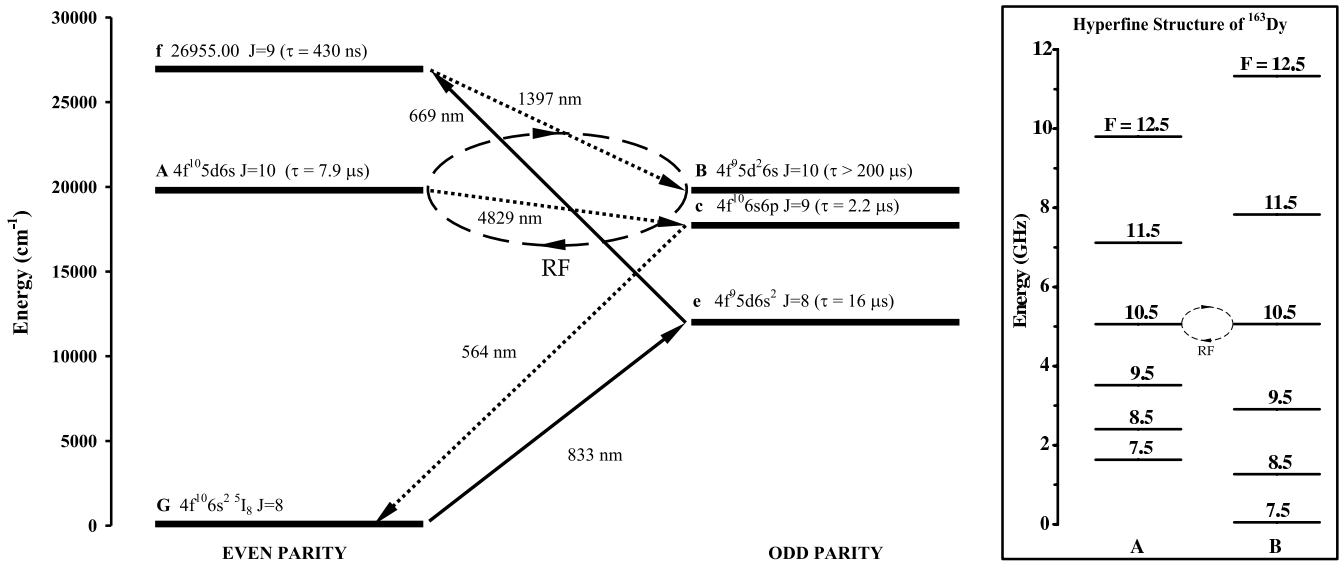


FIG. 1: Relevant levels and transitions in atomic dysprosium. Population and detection scheme: Level B is populated in a three-step process. The atoms are excited to level f in the first two steps using 833- and 699-nm laser light (solid arrows). The third step is a spontaneous decay (labeled by a short-dashed arrow) from level f to level B with $\sim 30\%$ branching ratio. The population is transferred to level A by the rf electric field (curved long-dashed lines). Atoms in level A decay to level c and then to the ground state. The fluorescence from the second decay (564 nm) is used for detection. Inset: Hyperfine structure of levels A and B for ^{163}Dy . Zero energy is chosen to coincide with the lowest hyperfine component.

difficult to interpret due to assumptions and systematic uncertainties. In fact, both the astrophysical evidence and the Oklo analysis are in disagreement with different quasar absorption measurements [15, 16] and earlier Oklo analyses [17, 18], respectively. These results have sparked interest in laboratory searches (see, for example, Refs. [19, 20, 21, 22]), which are easier to interpret but place weaker limits. The best laboratory limit of $|\dot{\alpha}/\alpha| < 1.2 \times 10^{-15}/\text{yr}$ was obtained from a comparison of a Hg^+ optical clock to a Cs microwave clock [20].

Recent calculations [23] have shown that the nearly degenerate opposite-parity levels in atomic dysprosium (Fig. 1, levels A and B) are highly sensitive to variations in α . In Ref. [11], a possible ultimate experimental sensitivity of $|\dot{\alpha}/\alpha| \sim 10^{-18}/\text{yr}$ was estimated for this system from an analysis of statistical and systematic uncertainties. In order to realize this level of sensitivity, the transition frequencies must be kept stable to a mHz level over a period of a year. Thus, knowledge of collisional shift rates is critical for the determination of the maximum allowable pressure in the vacuum chamber and, if necessary, for correction of the frequency measurements.

In Section II, we describe the technique used to measure transition frequencies and the procedure used during collisional-perturbation measurements. Section III presents the results and the details of the analysis. Section IV considers various systematic uncertainties. In Section V, we extract broadening and shift cross sections. In Section VI we present the implications for the α -variation experiment.

II. EXPERIMENTAL TECHNIQUE

A. Overview

The energy difference between the nearly degenerate levels considered in Refs. [23] and [11] are on the order of hyperfine splittings (Fig. 1 inset) and isotope shifts. Since Dy has seven stable isotopes, there are many rf transitions. The 235-MHz ^{162}Dy ($4f^9 5d^2 6s J=10 \rightarrow 4f^{10} 5d 6s J=10$) transition and the 3.1-MHz ($F=10.5 \rightarrow F=10.5$) transition are used for the α -variation experiment due to practical considerations such as high counting rate and low frequency, respectively. As shown in Fig. 1, the population transfer from the ground state to the long-lived ($\tau_B > 200 \mu\text{s}$ [24]) odd-parity level B requires three transitions. The first two transitions are induced via 833- and 669-nm laser light, while the last transition is a spontaneous decay with a $\sim 30\%$ branching ratio [25]. Atoms are transferred to the even-parity level A ($\tau_A = 7.9 \mu\text{s}$ [24]) with a frequency-modulated rf electric field referenced to a commercial Cs frequency standard. The transition frequency is determined via a lock-in technique by monitoring the 564-nm fluorescence.

B. Apparatus

In this section, we describe the atomic-beam apparatus, the optical setup, and the detection and pressure-measurement systems.

A detailed description of the atomic-beam source is

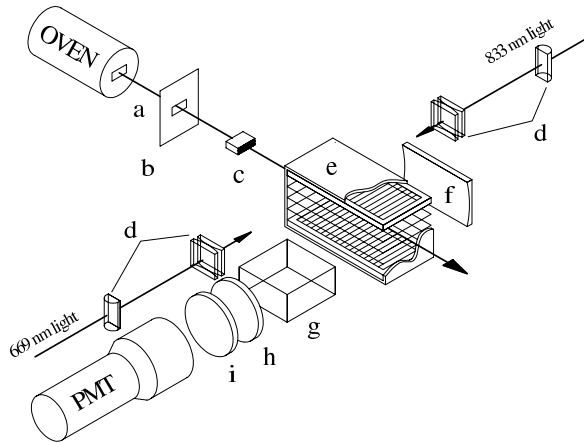


FIG. 2: Experimental setup (not shown to scale): a) Atomic beam produced by effusive oven source at ~ 1500 K; b) atomic-beam collimator; c) oven light collimator; d) cylindrical lenses to diverge laser beams; e) interaction region of atoms with the electric field enclosed in a magnetic shield (not shown); f) cylindrical mirror to collect fluorescent light; g) lucite light pipe; h) interference filter; and i) short-pass filter.

given in Ref. [25]. The beam is produced by an effusive oven with a multislit nozzle-array operating at ~ 1500 K. The oven consists of a molybdenum tube containing dysprosium metal, surrounded by resistive heaters made from tantalum wire inside alumina ceramic tubes. The radiation shielding is provided by five layers of tantalum sheets surrounding the oven and the heaters. In addition to the multislit nozzle, two external collimators are used to collimate the atomic beam and the oven light. The latter is necessary to minimize the background due to scattered oven light. The resulting atomic beam has a mean velocity of $\sim 5 \times 10^4$ cm/s with a full-angle divergence of ~ 0.2 rad ($1/e^2$ level) in both transverse directions.

The atoms enter the interaction region (Fig. 2), where they are first transferred to level B by two laser-induced transitions and a spontaneous decay. Approximately 600 mW of 833-nm light is produced by a Ti:Sapphire ring laser (Coherent 899) pumped by 15 W of Ar ion laser light (Coherent Innova 400). A ring dye laser (Coherent 699) with DCM [4-(Dicyanomethylene)-2-methyl-6-(*p*-dimethylaminostyryl)-4H-pyran] dye produces ~ 300 mW of 669-nm light. The dye laser is also pumped by an Ar ion laser (Coherent Innova 300) operating at 6 W of power.

Since the population transfer of a weakly collimated atomic beam due to narrow-band cw lasers is inefficient, an adiabatic passage technique is utilized to transfer atoms to level B. A detailed description of this technique and references to earlier work are given in Ref. [26]. Briefly, cylindrical lenses are used to diverge the two laser beams in the interaction region such that the divergences of the light beams match the atomic-beam divergence. Due to the Doppler effect, the atoms “see” a frequency chirp in laser detuning which adiabatically transfers the population to the excited state.

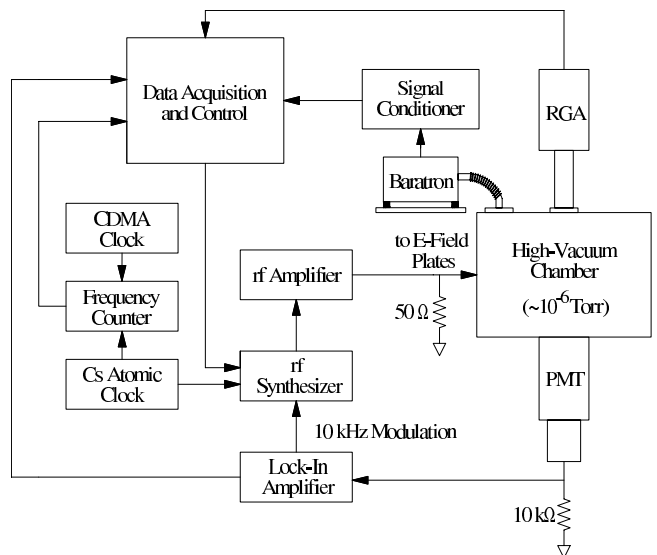


FIG. 3: Schematic diagram of the rf-generation, control, and pressure-measurement systems. The rf synthesizer is referenced to a Cs standard, which is compared to a CDMA (Code Division Multiple Access) primary reference source. Both clocks have a long term stability of $\sim 10^{-11}$. The output of the synthesizer is amplified and then sent to the electric-field plates and a 50Ω power-resistor termination in series with the larger impedance of the plates. The output of the photomultiplier tube is sent to the lock-in amplifier for detection and acquisition.

The rf electric field is formed between two parallel, 10 cm by 5 cm, wire grids made of 0.002 in Be-Cu wire. The separation between adjacent wires is 2.5 mm which minimizes surface area and hence surface-charge accumulation. The separation between the grids is ~ 2.5 cm. The entire assembly is enclosed inside a high-permeability magnetic shield which reduces the magnetic field in the interaction region to ~ 1 mG. The 564-nm fluorescence is collected by a lucite light pipe and detected with a photomultiplier tube (PMT) with bandpass interference and short-pass filters at the input window.

The rf-generation and detection system is shown in Fig. 3. The frequency-modulated rf field is generated by a synthesizer (Hewlett Packard 8647A) and sent through a 45-dB amplifier (ENI 604L). The rf power at the output is ~ 0.5 W. The synthesizer is referenced to a Cs frequency standard (Hewlett Packard 5061A) with a long term stability (>100 s) of 10^{-11} . This frequency standard is compared to a second clock (Symmetricom TS2700) to monitor its stability. A Signal Recovery 7265 lock-in amplifier provides a 10-kHz modulation signal to the rf synthesizer and demodulates the signal from the PMT. The signal from the lock-in along with the clock, pressure, and temperature data are sent to a computer for data acquisition.

The pressure measurement is provided by a residual gas analyzer (SRS RGA 200) and a capacitance manometer (MKS Baratron 690A.01). The residual gas analyzer (RGA) is used to monitor partial pressures of the background gasses. However, due to unknown gas-species-dependent sensitivity factors, it is not well suited to measuring the absolute pressure of various gases. The

manometer, on the other hand, is capable of absolute pressure measurement in a wide range of pressures from 0.1 Torr to a few μTorr with a resolution of 10^{-7} Torr. Measurements have shown that the manometer response is nonlinear below $10 \mu\text{Torr}$. Thus, the total manometer pressure was limited to $20 \mu\text{Torr}$ during the collisional-perturbation measurements. The manometer signal is processed by a signal conditioner (MKS 670B) which includes an active heater control mechanism to stabilize the operating temperature. To further reduce noise, the manometer is mechanically isolated by a vibration-isolation mount at the base and by the use of flexible bellows to connect to the vacuum chamber. The measured statistical uncertainty in the pressure range used during measurements is $\sim 1 \mu\text{Torr}$ for 100 seconds of integration.

C. Procedure

To minimize fluctuations such as those due to laser-power drifts or density fluctuations of the atomic beam, the rf voltage is frequency modulated at 10 kHz with an equal modulation depth (modulation index of 1). Since the rf-transition linewidth is ~ 20 kHz, this modulation provides a fast sweep across the absorption line shape. The outputs from the lock-in amplifier at the first and second harmonic of the modulation frequency are shown on Fig. 4. The first-harmonic signal is an odd function of detuning while the second-harmonic signal is an even function. It is well known that for small modulation amplitudes, the output signal at the harmonics of the modulation frequency are proportional to the corresponding derivatives of the absorption line shape [27]. In our system, since the modulation amplitude is comparable to the rf-transition linewidth, the harmonic signals contain higher derivative contributions. Therefore, a fitting function was derived from first-order time-dependent perturbation theory. This model does not include any effects due to power broadening or beam velocity distribution and is used to confirm qualitative behavior of the line shape.

To measure the transition frequency, the ratio of the first- and second-harmonic signals is used in order to reduce drifts further. The transition frequency is extracted from the ratio by a two-step process. First, the lock-in amplitude at the first and second harmonics and their ratio are recorded simultaneously [28] as the carrier frequency is scanned 4 kHz around the resonance. For such a small scan compared to the linewidth, the first harmonic is linear while the second harmonic is nearly a constant (Fig. 4). By fitting a linear function to the ratio, a conversion parameter from the ratio to frequency is obtained. Thus, these scans are called calibration files. Once the calibration is established, the rf carrier frequency is locked at a fixed value near resonance ($3,074,000$ Hz and $234,661,000$ Hz for the two transitions), and the ratio is measured repeatedly. These

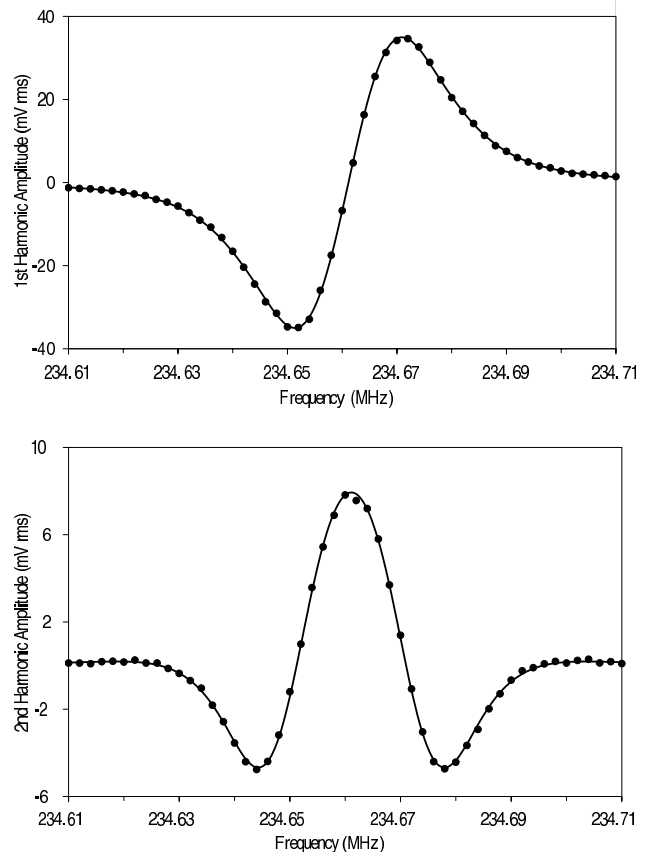


FIG. 4: First- and second-harmonic signals for 10-kHz frequency modulation. Solid line is a fit to the function derived from first-order time-dependent perturbation theory.

measurements are saved in the so-called fixed-frequency files. The average of ratios from these measurements are converted to frequency using the calibration file.

It should be mentioned that before recording a calibration file, a specific phasing procedure is used to maximize the lock-in-amplifier signal at both harmonics. Since Signal Recovery 7265 lock-in amplifier allows for separate phase adjustments for the two harmonics, the first-harmonic signal phase is adjusted to maximize the signal at 10 kHz above the fixed-frequency value, while the second-harmonic signal is maximized at the fixed frequency value. This procedure is used since the first- and second-harmonic signals are maximal near these frequencies, respectively. In addition, to minimize any instability or loss of signal due to laser detuning, each laser is retuned between recording data files by scanning over the laser resonances and setting the laser frequency to the resonance peak. Using this technique for frequency measurements, we have been able to achieve ~ 2 - and 6 -Hz statistical sensitivity for 1 second of integration time for the 235- and 3.1-MHz transitions, respectively.

For collisional-perturbation measurements, foreign gas is introduced into the chamber through a leak valve (Varian Model 1000). In order to minimize contamination, the hose connecting the gas cylinder to the leak valve

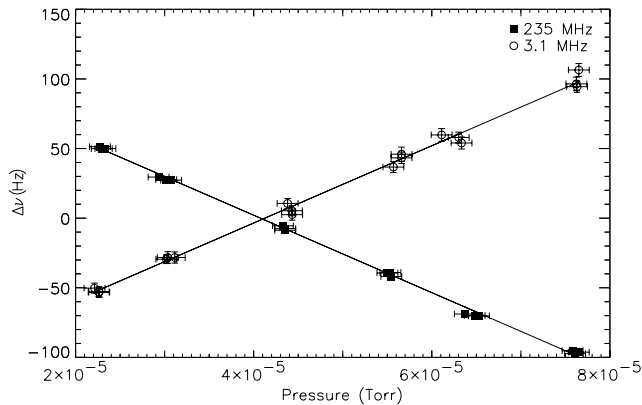


FIG. 5: Shift of the resonance frequency for both transitions due to the presence of Krypton. $\Delta\nu$ is the difference between the transition frequency and the fixed rf synthesizer carrier frequency (3,074,000 Hz and 234,661,000 Hz for the two transitions). The solid lines are the least-squares linear fits to the data.

is evacuated with a separate pump and flushed with gas several times prior to opening the valve. Then, the leak valve is opened and foreign gas is introduced continuously until a dynamic equilibrium is reached at a manometer pressure reading of $\sim 80 \mu\text{Torr}$. Meanwhile, the RGA is monitored for contamination due to other residual gases in the hose. After the background gas pressures drop below $10 \mu\text{Torr}$, measurements are taken at descending pressures between 80 and $20 \mu\text{Torr}$. At each pressure, one calibration and three fixed-frequency files are taken for each transition. To check for systematic drifts and signal loss, two more measurements at intermediate pressures are taken after the lowest-pressure measurement.

Since foreign gas is introduced from the top of the chamber while the chamber is continuously pumped from the bottom, a pressure gradient between the top and the interaction region might exist. Due to the large conductance of our chamber, we estimate a pressure gradient of $\sim 5\%$. This estimate is in agreement with the upper bound extracted from measurements taken with varying pumping speeds. Since the uncertainty in this pressure calibration error is not well known, this correction is not included in the results presented in Sec III and Sec. V in order to preserve the relative precision of the measurements.

III. ANALYSIS AND RESULTS

A. Frequency shifts

For all the gases except H_2 and Ne , which do not shift the transition frequency, ~ 100 Hz shifts were observed over the 10 to $80 \mu\text{Torr}$ pressure range. Since these transitions are between two excited states, the measured shift rates are due to the difference between the shift of the levels involved in the transition. As shown in Fig. 5,

TABLE I: Collisional-shift rates for the 235-MHz and 3.1-MHz transitions in the presence of various gases. The shift rates are expected to be equal and opposite for the two transitions since there is a change in sign between the energy difference of the levels involved. The O_2 coefficient was extracted using a measurement when air was let into the vacuum chamber. This was only performed for the 235-MHz transition. The results have been corrected for the presence of the background gases and the assigned errors include the effects of Dy self-shifts discussed in Sec. IV. As discussed at the end of Sec. II C, the analysis does not include the estimated 5% correction due to pressure calibration error.

	235-MHz Transition shift rates (Hz/ μTorr)	3.1-MHz Transition shift rates (Hz/ μTorr)
H_2	-0.02 ± 0.02	-0.09 ± 0.06
N_2	-1.71 ± 0.03	1.72 ± 0.05
O_2	-1.97 ± 0.25	-
He	1.25 ± 0.02	-1.27 ± 0.05
Ne	-0.01 ± 0.02	-0.02 ± 0.05
Ar	-2.21 ± 0.05	2.14 ± 0.07
Kr	-2.78 ± 0.05	2.78 ± 0.07
Xe	-2.74 ± 0.04	2.75 ± 0.07

the shifts for the two rf transitions are in opposite directions. This is expected since for the 235-MHz transition, level B is lower in energy than level A, while for the 3.1-MHz transition, the opposite is the case. Moreover, since electronic structures of the isotopes are identical, the absolute value of the shift coefficients should be identical, which is indeed the case within the precision of the experiment. For the gases that produce shifts, all but He , shift a given transition in the same direction.

The analysis of the shift data is complicated by the effects of background gases. Since the normal operating pressure of the vacuum chamber with the oven turned on is $\sim 5 - 10 \mu\text{Torr}$, the background gases, dominated mostly by H_2 and N_2 , and to a lesser extent by O_2 , make up a significant fraction of the overall pressure. Moreover, in some cases these gas pressures are not constant throughout a measurement [29] and contribute to the observed shift rates.

Since the capacitance manometer measures the total gas pressure in the chamber, RGA partial gas pressures are needed to establish the dominant-gas pressure and correct for the systematic shifts induced by the background gases. However, RGA partial pressures must be corrected with gas-species-dependent sensitivity factors that are not well determined. We have tried to extract these sensitivity factors using both data taken during collisional-perturbation measurements, where the oven is operating at ~ 1500 K, and auxiliary cold-oven measurements, where gas is introduced into the chamber with the oven turned off. In the latter case, the large H_2 background is absent, and the operating pressure of the vacuum chamber (without the foreign gas) is $\sim 1 \mu\text{Torr}$, dominated by N_2 . Therefore, the background gases can be ignored and the sensitivity factors extracted using lin-

ear fits to the manometer versus RGA data.

Extracting these parameters from the hot-oven data relies on the fact that during measurements where H_2 is introduced into the chamber, the N_2 and O_2 pressures are stable (we ignore all other gases including H_2O since their pressures are below 5×10^{-7} Torr throughout these measurements). Using this fact, the H_2 sensitivity factor, β_{H_2} , was extracted in the same way as the auxiliary cold-oven method, ignoring the other gases. The N_2 sensitivity factor, β_{N_2} , was extracted from measurements where N_2 was introduced into the chamber, but by accounting for the background H_2 pressure (using the extracted β_{H_2}). Finally, the O_2 sensitivity factor, β_{O_2} , was extracted taking both the N_2 and H_2 pressures into account using data where air was introduced into the chamber.

The RGA sensitivity factors extracted using the cold-oven and hot-oven data disagree at $\sim 10 - 20\%$ level, suggesting that they are also dependent on the background-gas pressures. As a result, in the rest of the analysis, sensitivity factors extracted from in-situ hot-oven measurements were used with larger error bars to accommodate for the results obtained by the auxiliary cold-oven measurements. In addition, in order to minimize the uncertainty introduced by the use of RGA sensitivity factors, the dominant gas pressures, P_{gas} , were calculated using

$$P_{\text{gas}} = P(\text{CM}) - \sum_i \beta_i P_i(\text{RGA}), \quad (1)$$

where $P(\text{CM})$ is the manometer pressure, $P_i(\text{RGA})$ and β_i are the RGA partial pressure and sensitivity factor of a background gas species i , respectively. Since the background-gas pressures are at least two times smaller than the dominant-gas pressure, by using this method, the uncertainty due to the sensitivity factors are reduced to levels comparable to or smaller than the manometer uncertainty of $1 \mu\text{Torr}$.

Once the sensitivity factors of the background gases were determined, an iterative approach was used to extract the Dy rf-transition-shift rates for H_2 , N_2 , and O_2 . The iterative approach is necessary for these gases because for a measurement where one of these gases dominates, the other two are background gases. As a result, to extract the correct shift rate for one of them requires the knowledge of the shift rates of the other two, which, in turn, are dependent on the shift rate that is being extracted. So, on the first iteration, the H_2 shift rate was extracted by taking into account the background N_2 and O_2 pressures but not the shifts due to them. Then, the N_2 shift rate was extracted similarly, by taking into account both the H_2 and O_2 pressures, as well as shifts due to H_2 . Finally, the O_2 shift rate was extracted by taking into account both N_2 and H_2 pressures and shifts (only for the 235-MHz transition since no air data were taken for the 3.1-MHz transition). Then, these first-order coefficients were used to extract higher-order coefficients where pressures and shifts due to all the background gases were used

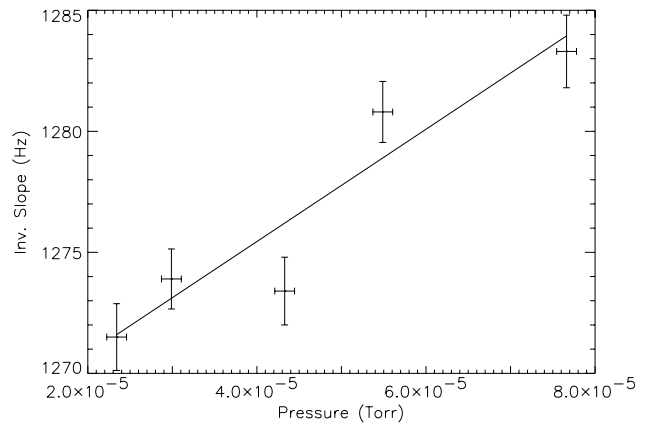


FIG. 6: Collisional broadening for the 235-MHz transition due to Kr without the phasing-effect correction. On the y axis, the inverse of the normalized first harmonic slope, which is directly proportional to the linewidth is plotted. The solid line is the least-squares linear fit to the data.

in every step. This iterative process converged within three iterations, improving χ^2 at every step.

The rest of the gases were easier to analyze since they do not appear as background gases in other measurements. The coefficients for these gases were determined by taking into account the background H_2 , N_2 and O_2 . For the 3.1-MHz transition, the O_2 shift rate for the 235-MHz transition with the opposite sign was used. The results are presented in Table I.

B. Broadening

Since the main focus of this study is frequency shifts, the experimental technique we utilize is optimized for frequency measurements. Nevertheless, the broadening rates can also be extracted from the calibration files. However, determination of the broadening rates is more difficult than the shift rates since, as discussed below, the sensitivity of the calibration data to linewidth is low. In addition, there is a systematic effect caused by the phasing procedure used (see Sec. II C) coupled with the collisional shift of the resonance frequency that results in an enhancement of apparent broadening rates for one transition and reduction for the other.

The slope of the first-harmonic signal near resonance, normalized by the second harmonic can be extracted by fitting a linear function to the ratio from the calibration file data, as described in Sec. II C. For small modulation amplitudes, the first-harmonic signal is proportional to the first derivative of the absorption line shape and the second harmonic to the second derivative. Near resonance, to first order in frequency detuning, both of these functions have a $1/\gamma^3$ dependence. As a result, the slope of the ratio is insensitive to the linewidth. However, in our system the modulation amplitude is comparable to the linewidth, and the harmonics contain higher-order

TABLE II: Collisional broadening rates for the 235-MHz transition in the presence of various gases. The large uncertainties are due to statistical noise and the uncertainty in the conversion factor from the inverse slope to linewidth. The O₂ result is presented as an upper bound at 2 σ confidence level. The results do not include the estimated 5% uncertainty due to pressure gradients in the chamber.

	235-MHz Transition broadening rates (Hz/ μ Torr)
H ₂	8.6 ± 1.9
N ₂	3.0 ± 1.7
O ₂	< 8.6
He	5.3 ± 1.9
Ne	1.4 ± 1.3
Ar	4.9 ± 1.4
Kr	5.3 ± 1.4
Xe	2.8 ± 2.0

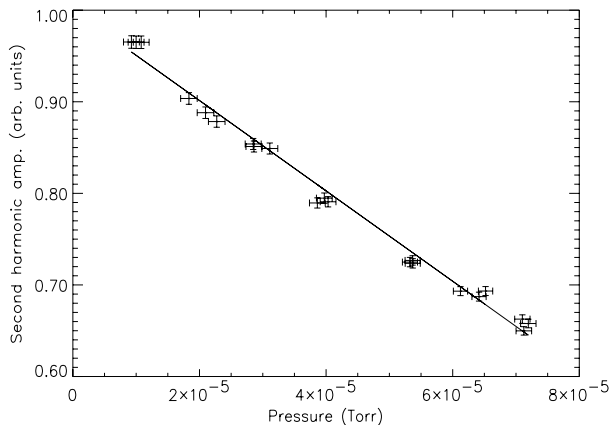


FIG. 7: Decrease in the second harmonic signal for the 235-MHz transition due to Xe. The signal has been normalized to one at zero pressure. The solid line is the least-squares fit to the data.

derivatives which result in a small dependence of the slope on the linewidth. In practice, the inverse of this slope is the useful quantity in converting the ratio to frequency. It is proportional to the linewidth for small changes in the linewidth [30] and increases with gas pressure due to pressure broadening (Fig. 6).

The conversion factor from the inverse slope to linewidth is extracted from measurements where calibration files and line-shape scans were taken simultaneously for different rf input powers, which lead to power broadening. The extracted conversion factor of 31(5) agrees with the conversion factor of 28.2 obtained from the first-order perturbation theory calculation by linearizing the ratio near resonance. In the analysis of the data, the experimental value is used and errors propagated accordingly.

There is a systematic effect related to the phasing procedure which is due to the dependence of the first-harmonic slope near resonance, and hence the slope of

the ratio, on the frequency at which the phase is adjusted to maximize the signal (which we define as phasing frequency). For small changes in the phasing frequency, the experimental measurements show a linear dependence with 0.025(3) and 0.029(5) Hz change in the inverse slope per Hz change in the phasing frequency for the 235- and 3.1-MHz transitions, respectively. For all the gases where shifts are observed, with the exception of He, which shifts the transition frequency in the opposite direction, this effect leads to an enhancement of the broadening rates for the 235-MHz transition and a reduction for the 3.1-MHz transition. This is due to the fact that as the gas pressure is changed, the transition frequency shifts but the phasing frequency is fixed at 10 kHz above the carrier frequency used for the fixed-frequency measurements. As a result, the phasing frequency changes with respect to the transition frequency. For example, from the Kr shift data shown in Fig. 5, at low pressures, the rf carrier frequency for the 235-MHz transition is 50 Hz below the transition frequency, while at high pressures, it is 100 Hz above the transition frequency (the y axis of the figure is transition frequency minus carrier frequency). As a result, while at low pressures, the phasing frequency with respect to the transition frequency is less than 10 kHz, at high pressures, it is greater than 10 kHz. This leads to an enhancement of apparent broadening since at low pressures the observed inverse slope is less than the value that would be observed without this effect, and the opposite is the case at high pressures. The 3.1-MHz transition is shifted in the opposite direction, and as a result, the observed broadening is reduced for this transition. This is a significant effect since the changes in the transition frequency lead to 3 - 4 Hz changes in the inverse slope. In comparison, as seen in Fig. 6, the changes in the inverse slope due to the gases are 10 - 15 Hz.

The results that have been corrected for this systematic effect, as well as the systematic effect due to the presence of the background gases, are presented in Table II. Even with this correction, the statistical noise coupled with the uncertainty in the conversion from inverse slope to linewidth lead to poor fits for the 3.1-MHz data. Consequently, the broadening results for this transition are not presented. For the same reasons, only an upper bound for the 235-MHz O₂ broadening rate is presented. Due to small O₂ pressure variation ($\leq 1.1 \mu$ Torr), the omission of the O₂ correction is not problematic in this case since even if the broadening rate for O₂ were 8.6 Hz/ μ Torr (the upper 2 σ bound from Table II), this would lead to an error of $\lesssim 5\%$ for the measurements that exhibit the largest O₂ pressure variation.

C. Signal Attenuation

During the fixed-frequency measurements, $\sim 15 - 40\%$ decrease in the second-harmonic-signal amplitude, which is nonzero at resonance, as a function of foreign-gas pressure was observed (Fig. 7). This signal attenuation can

TABLE III: Signal-attenuation rates for the 235-MHz and 3.1-MHz transitions and upper bounds for collisional quenching cross sections in the presence of various gases. The results have been corrected for the presence of the background gases and the assigned error bars include systematics due to beam-density variations. The results do not include the estimated 5% uncertainty due to pressure gradients in the chamber. For the combined cross sections, gas temperature of 300(5) K and Dy beam temperature of 1500(50) K are assumed.

	235-MHz Transition ϵ (10^{-3} 1/ μ Torr)	3.1-MHz Transition ϵ (10^{-3} 1/ μ Torr)	Quenching $\langle\sigma_q v\rangle$ (10^{-10} cm ³ /s)
H ₂	4.1 \pm 0.2	3.9 \pm 0.2	< 13
N ₂	4.4 \pm 0.5	4.3 \pm 0.7	< 14
O ₂	10 \pm 1	-	< 32
He	2.6 \pm 0.2	2.6 \pm 0.2	< 8
Ne	2.3 \pm 0.2	2.6 \pm 0.2	< 7.6
Ar	3.3 \pm 0.3	3.7 \pm 0.2	< 11
Kr	3.9 \pm 0.2	4.0 \pm 0.2	< 13
Xe	4.9 \pm 0.2	5.2 \pm 0.2	< 16

be attributed to either decrease in the beam density due to elastic scattering or decrease in the fluorescence intensity due to inelastic quenching. The signal amplitude decreases with the distance the beam travels through the foreign gas:

$$\langle S(v) \rangle = G I_0 \langle e^{-l/\lambda(v)} \rangle, \quad (2)$$

where G is the efficiency of the detection system, I_0 is the fluorescence intensity at zero pressure, λ is the mean free path, and l is the beam path length through the foreign gas. Here, $\langle \dots \rangle$ denotes average over the beam velocity distribution. Since λ is inversely proportional to pressure, the signal for small pressures can be written as:

$$\frac{\langle S(v) \rangle}{S_0} = \langle e^{-l/\lambda(v)} \rangle \approx \langle 1 - l/\lambda(v) \rangle = (1 - \epsilon p), \quad (3)$$

where S_0 is the second-harmonic signal at zero pressure, and ϵ is the attenuation rate.

The analysis of the quenching data is similar to the analysis of the shift and broadening. First, the iterative process was used for the dominant gases in the background, H₂, N₂, and O₂. Then, the values extracted were used in the analysis of the remaining gases. The attenuation rates tabulated in Table III include systematic corrections due to clogging of the unheated photon collimator (Fig. 3) and temperature drift of the ovens. To detect any changes in the signal amplitude due to clogging, the two measurements at intermediate pressures taken after the lowest pressure points, as discussed in Sec. II C, were used. The oven temperature was monitored by a thermocouple and changes in the beam density due to temperature fluctuations were estimated using Dy saturated vapor-pressure dependence on temperature (see Sec. IV.)

The interpretation of the signal attenuation data is complicated since it is difficult to separate elastic scattering events that decrease beam density from inelastic quenching that decreases the population of level B. Nevertheless, we expect the elastic scattering contribution to

be small since although typical elastic cross sections are $\sim 10^{-14}$ cm² (corresponding to a mean free path of ~ 30 cm at 100 μ Torr), large angle scattering necessary for significant collimation loss is suppressed by more than one order of magnitude due to the fact that differential cross section is sharply peaked at small scattering angles [31]. Using the results derived in Ref. [32] for hard-ball scattering, we have estimated that the differential cross section becomes appreciable below 0.1 - 0.01 radian in the center-of-mass frame. For a head-on collision, this results in 6 - 7 mrad deviation for the Dy beam in the laboratory frame. This deviation is small compared to the collimation half angle of 0.1 radian used in our experiment. However, since this estimate uses a hard-ball model, which depends on few assumptions such as a specific minimum distance between the centers of the spheres, as opposed to more complicated interactions such as quasi-molecular formation, it can vary by a multiplicative factor of 2 - 5. As a result, we only present upper bounds for the inelastic quenching cross sections.

The attenuation rates can be related to the quenching cross sections through a characteristic mean free path, which can be expressed as

$$\tilde{\lambda} = \frac{\langle v_B \rangle}{n_G \langle \sigma_q v \rangle} \quad (4)$$

where $\langle v_B \rangle = 3/4(2\pi k T_B/m_B)^{1/2}$ is the average beam velocity given by a modified Maxwellian distribution, n_G is the density of foreign gas, v is the relative velocity of the gas and beam particles, and $\langle \sigma_q v \rangle$ denotes an average over both the gas and the beam velocity distributions.

Using Eq. (4) and Eq. (3), the quantity $\langle \sigma_q v \rangle$ can be written in terms of ϵ as

$$\langle \sigma_q v \rangle = \frac{3}{4} \sqrt{\frac{2\pi k}{m_{Dy}}} \frac{k \epsilon}{l} T_G T^{1/2}, \quad (5)$$

where T_G and T are the temperatures of the foreign gas and the oven, respectively. The path length, l , is not well

defined in our experimental setup. Since the light pipe has a width of 6.7 cm, it collects fluorescence from atoms at various path lengths. The tabulated results assume a path length of 5.5 cm, which is the distance between the laser excitation region and the center of the light pipe. The results are summarized in Table III.

IV. SYSTEMATIC UNCERTAINTIES

In addition to systematic effects considered above, Dy*(excited Dy atoms)-Dy* and Dy*-Dy collisions within the beam can lead to a systematic change in the transition frequency and linewidth, if the beam density does not remain constant during the collisional measurements. We have performed independent measurements of self-collisions in our system and present here an estimate of their contribution to the systematic uncertainty.

The beam density can be controlled by varying the oven temperature. The temperature dependence of Dy saturated-vapor pressure is given by the following empirical formula [33]:

$$P = 10^{12.460 - 15336/T - 1.114 \log(T)}, \quad (6)$$

where P is the pressure in Torr and T is the temperature in Kelvin.

We have varied the oven temperature, which was monitored by a thermocouple, from 1077°C to 1170°C, while monitoring the frequency for both transitions. This temperature range corresponds to a Dy density of $(0.3 - 1.5) \times 10^{14} \text{ cm}^{-3}$ in the oven. Earlier absorption measurements [25] have shown that the density of atoms in the population and detection region is $\sim 5 \times 10^9 \text{ cm}^{-3}$ at the normal operating temperature of 1170°C. This density is in agreement with estimates based on effusive flow. To obtain the Dy density in the interaction region for various temperatures, the scaling factor between the calculated density in the oven at 1170°C and the absorption measurements was applied uniformly to all the calculated densities. The extracted self-shift rates were $0.2(2.0) \times 10^{-10} \text{ Hz cm}^3$ and $-3.1(6.0) \times 10^{-10} \text{ Hz cm}^3$ for the 235-MHz and 3.1-MHz transitions, respectively (Fig. 8). An upper bound for the magnitude of the self-shift rate can be estimated by noting that the rates, m , for these two transitions should be the same in magnitude but opposite in sign:

$$\begin{aligned} |m| &= \frac{1}{2} |m_{235} - m_{3.1}|, \\ 0 &= |m_{235} + m_{3.1}|, \end{aligned} \quad (7)$$

where the second equation provides a way to estimate errors. The resulting upper bound on the magnitude of the self-shift rate is $< 4.9 \times 10^{-10} \text{ Hz cm}^3$ at 1σ confidence level. Since changing the oven temperature does not discriminate between Dy* and Dy densities, this upper bound is an effective rate due to both Dy*-Dy* and

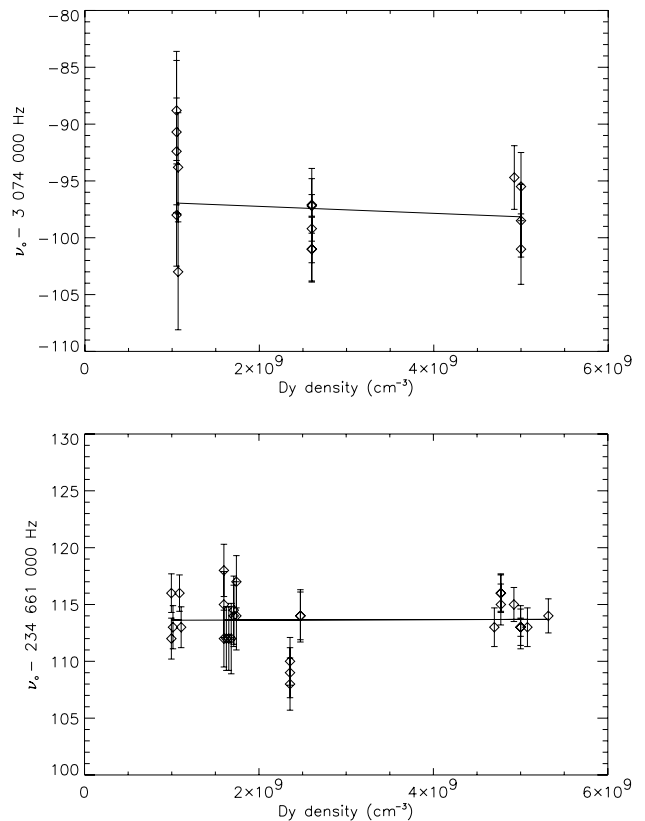


FIG. 8: Shifts due to collision of the Dy atoms in the beam. Beam density was varied by changing the oven temperature from 1170°C to 1077°C which correspond to the estimated atomic densities in the interaction region shown in the plots.

Dy*-Dy collisions. A simple way to address this ambiguity would be to change the laser powers simultaneously to change the fraction of excited Dy atoms. This method may be pursued in a future study.

Using the extracted upper bound, we can estimate the systematic contribution of self-collisions to the measured shift and broadening rates. This requires a mechanism that changes Dy beam density as a function of foreign-gas pressure. As a worst-case scenario, we assume that all of the observed signal attenuation is due to the decrease in the Dy density as a result of scattering with the foreign-gas atoms. Depending on the gas, this results in a change of $\sim (0.9 - 2.2) \times 10^9 \text{ cm}^{-3}$ in the Dy density, which corresponds to $\sim 0.4 - 1.1 \text{ Hz}$ change in the magnitude of the transition frequency from low to high pressures. The correction to the foreign-gas shift rates are in the range of $0.005 - 0.01 \text{ Hz}/\mu\text{Torr}$. These uncertainties have been included in Table I.

Since, in general, broadening should be of the same order of magnitude as shifts, the uncertainty due to self-broadening is negligible compared to the errors quoted on Table II.

TABLE IV: Collisional shift and broadening cross sections and their ratios at foreign-gas temperature of 300(5) K. The shift cross sections for the two transitions have been combined into a single result with the following sign convention: a positive frequency shift for the 3.1-MHz transition gives a positive cross section.

	$\langle\sigma_s v\rangle$ (10^{-10} cm ³ /s)	$\langle\sigma_b v\rangle$ (10^{-10} cm ³ /s)	$\langle\sigma_s v\rangle/2 \langle\sigma_b v\rangle$
H ₂	0.05 ± 0.04	8.4 ± 1.9	0.003 ± 0.002
N ₂	3.34 ± 0.07	2.9 ± 1.7	0.6 ± 0.3
O ₂	3.9 ± 0.5	< 8.4	< 0.2
He	-2.44 ± 0.05	5.2 ± 1.9	-0.2 ± 0.1
Ne	0.02 ± 0.04	1.4 ± 1.3	0.01 ± 0.02
Ar	4.3 ± 0.1	4.8 ± 1.4	0.4 ± 0.1
Kr	5.4 ± 0.1	5.2 ± 1.4	0.5 ± 0.1
Xe	5.3 ± 0.1	2.7 ± 2.0	1.0 ± 0.7

V. DISCUSSION

The adiabatic impact approximation results give a Lorentzian line shape with the transition frequency and linewidth modified by [34]:

$$\Delta\gamma = \frac{1}{2\pi}(2n \langle v\sigma_b \rangle) = \frac{\langle v\sigma_b \rangle}{\pi kT} p, \quad (8)$$

$$\Delta\nu = \frac{1}{2\pi}(n \langle v\sigma_s \rangle) = \frac{\langle v\sigma_s \rangle}{2\pi kT} p, \quad (9)$$

where k is the Boltzmann constant, p and T are the foreign-gas pressure and temperature, $\langle\dots\rangle$ denotes an average over both the gas and the beam velocity distributions. The shift and broadening cross sections are given by (see, for example, Ref. [35]):

$$\sigma_s = 2\pi \int_0^\infty b \sin(\phi(b)) db, \quad (10a)$$

$$\sigma_b = 2\pi \int_0^\infty b(1 - \cos(\phi(b))) db. \quad (10b)$$

Here, $\phi(b)$ is the induced phase shift which depends on the form of the interaction potential. These potentials are usually expressed as $V_k = C_n^k/r^n$ for the k^{th} excited state with the van der Waals ($n=6$) being the primary long range interaction for neutral atoms. For this potential, the collisional cross sections for a transition between arbitrary states a and b are given by

$$\langle\sigma_b\rangle = 2\pi(0.602) \left(\frac{3\pi|C'_6|}{8 \langle v \rangle}\right)^{2/5}, \quad (11a)$$

$$\langle\sigma_s\rangle = \text{sign}(C'_6) 2\pi(0.438) \left(\frac{3\pi|C'_6|}{8 \langle v \rangle}\right)^{2/5}, \quad (11b)$$

where $C'_6 = (C_6^a - C_6^b)/\hbar$.

As illustrated by this example, $\sigma_s/2\sigma_b$ has a value of 0.364, independent of C'_6 . In fact, within the adiabatic impact approximation, a unique ratio is predicted for each interaction potential which can be used to determine the dominant form of the interaction. Since cross sections can have a dependence on the relative velocities, the quantities $\langle\sigma v\rangle$ for both broadening and shifts extracted from our experimental results are tabulated in

Table IV, as well as their ratio [36]. The sign convention for the shift cross sections has been chosen such that a positive frequency shift for the 3.1-MHz transition (where level B has higher energy than level A) gives a positive cross section. The measured ratios vary widely for different gases. In foreign gas perturbations, this is a common situation since in addition to long range attractive interactions, short range repulsive forces can be important. This is especially true for H₂, He and Ne which do not interact strongly via the van der Waals interaction [37]. Our results are in agreement with this trend: H₂ and Ne cause no shifts, while He induces an opposite shift as a result of dominant repulsive forces. On the other hand, all three gases show broadening comparable to the other gases. This can be understood by observing the integrands of Eqs. (10). While the integrand for the shift cross section oscillates around zero, the integrand for the width cross section is always positive, yielding a nonzero broadening even for short-range interactions.

VI. IMPLICATIONS FOR THE α -VARIATION EXPERIMENT

Collisional shifts are one of the most important systematics for an experiment searching for the temporal variation of α using Dy since they mimic frequency shifts that would be induced by variation in α . The α dependence of different isotopes and hyperfine-level manifolds of odd isotopes are the same [38]. As a result, the entire manifold of level B shifts identically with respect to the manifold of level A. Monitoring different transitions where energy of level A is larger than the energy of B, and vice versa provides a powerful tool in detecting and eliminating certain systematics since the shift induced by α variation should have the same magnitude but opposite sign for these transitions. However, as seen in Table I, this behavior is identical to that of the shifts induced by collisions, and therefore, gas pressures must be kept stable to 1 part in 10^4 for a background pressure of $\sim 1 \mu\text{Torr}$, or lowered to $\lesssim 3 \times 10^{-10}$ Torr to achieve the desired mHz-level stability over a year.

This conclusion is in agreement with the estimates pro-

vided in Ref. [11]. However, it was also argued in Ref. [11] that a suppression of collisional shifts might exist due to the fact that the transitions are nominally between f and d inner-shell electrons and that inelastic quenching might remove atoms experiencing collisions from levels A or B so that they would not contribute to the signal. Our present results do not reveal such suppression of collisional shifts.

With the current experimental setup, the operating pressure is $\sim 5 \mu\text{Torr}$, mostly dominated by hydrogen and nitrogen. A new vacuum chamber that can achieve 10^{-10} Torr with a Dy oven operating at 1500 K is under construction. In the mean time, data that is being acquired with the current chamber will be corrected using the measured collisional shift coefficients to achieve an estimated stability of 2 Hz over a year, which corresponds to sensitivity of $|\dot{\alpha}/\alpha| \sim 10^{-15}/\text{yr}$. This sensitivity is comparable to the best current laboratory limits [20, 22].

VII. CONCLUSION

In summary, we have reported collisional shift and broadening rates, and cross sections for radio-frequency transitions between excited states of ^{162}Dy and ^{163}Dy in the presence of 10 to 80 μTorr of H_2 , N_2 , O_2 , He, Ne, Ar,

Kr, and Xe. In addition, we have placed upper bounds on quenching cross sections using the pressure dependence of the signal amplitude. A frequency-modulation technique used for the search of the temporal variation of the fine-structure constant was utilized to measure the small perturbations induced at such low pressures. The extracted cross sections are similar to cross sections for optical transitions [8].

To improve our understanding of the interaction potentials, several avenues may be pursued in the future. As seen in Eqs. (11), the possible velocity dependence of cross sections can be exploited by varying the gas temperature. Moreover, a careful study of the line shape far off resonance would be informative due to strong temperature dependences and satellite-line formations at higher pressures [37].

Acknowledgments

We thank V. V. Yashchuk, A. Lapierre, D. F. Kimball, D. English, J. E. Stalkner, and W. Gawlik for valuable discussions. We are grateful to E. D. Commins for his support and encouragement. This work was supported in part by the UC Berkeley-LANL CLC program and NIST Precision Measurement Grant.

-
- [1] A. A. Michelson, *Astrophys. J.* **2**, 251 (1895).
 - [2] H. A. Lorentz, *K. Acad. Wet.* **8**, 591 (1906).
 - [3] V. Weisskopf, *Phys. Z.* **34**, 1 (1933).
 - [4] E. Lindholm, *Ark. Mat. Astr. Fys.* **28B**, 3 (1941).
 - [5] H. M. Foley, *Phys. Rev.* **69**, 616 (1946).
 - [6] H. G. Khun, *Philos. Mag.* **18**, 987 (1934).
 - [7] S. Ch'en and M. Takeo, *Rev. Mod. Phys.* **29**, 20 (1957).
 - [8] N. Allard and J. Kielkopf, *Rev. Mod. Phys.* **54**, 1103 (1982).
 - [9] J. Szudy and W. E. Baylis, *Phys. Rep.* **266**, 127 (1996).
 - [10] C. Hancox et al., *Nature* **431**, 281 (2004).
 - [11] A. T. Nguyen, D. Budker, S. K. Lamoreaux, and J. R. Torgerson, *Phys. Rev. A* **69**, 22105 (2004).
 - [12] J. K. Webb et al., *Phys. Rev. Lett.* **87**, 091301 (2001).
 - [13] M. T. Murphy et al., *Mon. Not. R. Astron. Soc.* **345**, 609 (2003).
 - [14] S. K. Lamoreaux and J. R. Torgerson, *Phys. Rev. D* **69**, 121701(R) (2004).
 - [15] R. Quast et al., *Astron. Astrophys.* **415**, L7 (2004).
 - [16] R. Srianand et al., *Phys. Rev. Lett.* **92**, 121302 (2004).
 - [17] T. Damour and F. Dyson, *Nucl. Phys.* **B480**, 37 (1996).
 - [18] Y. Fujii et al., *Nucl. Phys.* **B573**, 377 (2000).
 - [19] H. Marion et al., *Phys. Rev. Lett.* **90**, 150801 (2003).
 - [20] S. Bize et al., *Phys. Rev. Lett.* **90**, 150802 (2003).
 - [21] M. Fischer et al., *Phys. Rev. Lett.* **92**, 230802 (2004).
 - [22] E. Peik et al., *Phys. Rev. Lett.* **93**, 170801 (2004).
 - [23] V. A. Dzuba, V. V. Flambaum, and M. V. Marchenko, *Phys. Rev. A* **68**, 022506 (2003).
 - [24] D. Budker, D. DeMille, E. D. Commins, and M. Zolotarev, *Phys. Rev. A* **50**, 132 (1994).
 - [25] A. T. Nguyen, D. Budker, D. DeMille, and M. Zolotarev, *Phys. Rev. A* **56**, 3453 (1997).
 - [26] A. T. Nguyen, G. D. Chern, D. Budker, and M. Zolotarev, *Phys. Rev. A* **63**, 013406 (2000).
 - [27] W. Demtröder, *Laser Spectroscopy: Basic Concepts and Instrumentation* (Springer, 2003), 3rd ed.
 - [28] Signal Recovery Model 7265 lock-in amplifier is capable of providing both harmonics and their ratio simultaneously through digital signal processing.
 - [29] This is mainly true for N_2 and O_2 due to residual air in the hose connecting the gas cylinder to the leak valve that is introduced into the chamber with the foreign gas.
 - [30] The function relating the linewidth to inverse slope is nonlinear in general, but for small changes, as in the case of present measurements, it can be linearized. As a result of this linearization, in addition to the multiplicative conversion factor, there is a large, unphysical y-intercept that must be used to convert inverse slopes to linewidths. However, this y-intercept is irrelevant for the extraction of the broadening rates since it is independent of pressure.
 - [31] N. F. Ramsey, *Molecular Beams* (Clarendon Press, Oxford, 1990).
 - [32] H. S. W. Massey and C. B. O. Mohr, *Proc. Roy. Soc. A* **141**, 434 (1933).
 - [33] D. R. Lide, ed., *CRC Handbook of Chemistry and Physics* (CRC Press, Cleveland, 1999).
 - [34] The additional factor of two in the linewidth comes from the definition of the Lorentzian line shape which is proportional to $1/((\omega - \omega_0)^2 + (\gamma/2)^2)$.
 - [35] I. I. Sobel'man, L. A. Vainshtein, and E. A. Yukov, *Excitation of Atoms and Broadening of Spectral Lines*

(Springer, 1995), 2nd ed.

- [36] Strictly speaking, $\langle\sigma v\rangle$ differs from $\langle\sigma\rangle\langle v\rangle$ obtained from Eqs. (11) by a geometrical correction factor (see, for example, K. Berkling et al., *Z. Physik* **166**, 406 (1962)). However, since both σ_b and σ_s have the same velocity dependence, the difference disappears in the ratio of the
- two cross sections.
- [37] A. Corney, *Atomic and Laser Spectroscopy* (Clarendon Press, Oxford, 1988).
- [38] There are differences due to hyperfine interactions, but these are suppressed by a factor of m_e/m_p .